STUDIA UBB CHEMIA, LXXI, 1, 2026 (p. 57-75)
(RECOMMENDED CITATION)
DOI:10.24193/subbchem.2026.1.05

CFD PARTICLE MODEL AND OPTIMIZATION OF THE REACTION OF SULFIDIC PELLETS WITH HYDROGEN

Vlad-Cristian SANDU[a], Alexandru-Constantin BOZONC[a], Ana-Maria CORMOS[a,*], Shareq Mohd NAZIR[b], Paul COBDEN[c]

ABSTRACT. A dynamic 2D CFD multilayer particle model was developed and simulated using COMSOL Multiphysics 6.3 to study desulfurization of copper sulfide (Cu_2S) with hydrogen (H_2). The model solved interstitial velocity and pressure fields in the gas phase coupled to transiently resolved species transport in both gas and solid phases, incorporating reduction kinetics and dynamic pellet porosity change. After model validation with experimental data from literature, a constricted optimization study was carried out to identify optimal conditions necessary to maximize Cu_2S conversion and H_2 utilization. The optimization solutions (i.e., 100% H_2 and 973 K) indicated that both high inlet mole fraction of H_2 and temperature improved the objective function steadily, highlighting the trade-off between maximizing conversion and minimizing H_2 slip. The current work can serve as a framework for reactor-scale simulations aimed at intensification and decarbonization of primary copper production.

Keywords: *copper sulfide, hydrogen desulfurization, CFD multilayer particle model, process optimization*

INTRODUCTION

Despite global initiatives to limit climate change, annual greenhouse gas (GHG) emissions continue to increase steadily every year. Energy-related carbon dioxide (CO_2) emissions reached an all-time high in 2024 of

[a] *Babeş-Bolyai University, Faculty of Chemistry and Chemical Engineering, 11 Arany Janos str., RO-400028, Cluj-Napoca, Romania.*
[b] *KTH Royal Institute of Technology, Department of Chemical Engineering, Brinellvägen 8, Stockholm, Sweden.*
[c] *Swerim AB, Box 812, 971 25 Luleå, Sweden.*
[*] *Corresponding author: ana.cormos@ubbcluj.ro*

37.8 Gt CO_2, 0.8% higher than the previous year, contributing to record concentrations of CO_2 in the atmosphere of 442.5 ppm [1]. Although emissions from industrial processes declined by 2.3% in 2024, further decarbonization of industry is necessary to stay within the proposed carbon budget to keep global warming from exceeding 1.5 °C above pre-industrial levels [2].

Copper (Cu) is an essential component in many technologies supporting global decarbonization, including renewable energy generation (i.e., PV panels and generators), energy storage (i.e., batteries), electric vehicles (i.e., motors and wiring), power transmission and distribution, etc. In 2024, the production of Cu accounted for 0.2% of global anthropogenic GHGs [3], although estimates see the Cu cycle contributing up to 2.7% by 2050 without efforts to reduce emissions [4]. The current demand for Cu at 25 Mt per year is projected to double by 2035 [5], with energy transition technologies accounting for half of the demand [6]. Consequently, the Cu sector is in the position of having to expand production to support the overall energy transition while also reducing its own emissions in accordance with global decarbonization goals.

There are two main routes for Cu production, pyrometallurgical and hydrometallurgical, depending on the properties of the raw material. Pyrometallurgy, accounting for around 80% of copper mine production, is the dominant route for sulfide ores, especially chalcopyrite, while hydrometallurgy is preferred for low-grade oxide ores and some secondary sulfides, since chalcopyrite is extremely difficult to dissolve in aqueous solutions [7]. The pyrometallurgical route, shown in Figure 1, is an inherently multi-stage process of higher complexity when compared to hydrometallurgy (i.e., leaching, extraction, stripping and electrowinning) which involves fewer high-temperature unit operations to produce high-purity copper cathodes from low-grade ores that pyrometallurgy cannot handle efficiently [8]. From an environmental perspective, pyrometallurgy must manage SO_2-rich off-gases from the smelting and converting stages by capturing and converting them into sulfuric acid. On the other hand, key environmental issues in hydrometallurgy include management of (i) solution acidity to protect groundwater by utilizing adequate liners and (ii) acid mist formation in the electrowinning stage by using ventilation systems or suppressants [9]. From an economic point of view, a higher capital investment is necessary for copper refinement via pyrometallurgy (i.e., fixed investment of 33,000 $ per annual t Cu produced) vs. the hydrometallurgical route (i.e., fixed investment of 3,550 $ per annual t Cu produced), attributed to much smaller infrastructure requirements for the latter [9]. Operating costs for both routes are mainly driven by electricity price, due to the power intensive smelting and electrowinning stages, with higher overall costs for pyrometallurgy (i.e., 6 $ per kg Cu produced) vs. hydrometallurgy (i.e., 2 $ per kg Cu) [9].

Production from primary sources via pyrometallurgy begins with extraction of Cu-bearing ores from mines, typically containing between 0.25 – 1 wt.% Cu. The sulfide ore is first crushed and ground, then subjected to flotation to obtain Cu concentrate with 20 – 40 wt.% Cu. The concentrate is then smelted in a flash furnace at temperatures of 1200 – 1300 °C, resulting in Cu matte containing 50 – 70 wt.% Cu. Subsequently, the matte is further refined and converted to blister Cu with 98.5 – 99.5 wt.% Cu. A final electrochemical process results in refined Cu cathodes with higher than 99.99% purity. In addition to raw ore, Cu scrap can be introduced into the pyrometallurgical production process at different stages, but can also be processed as a standalone feedstock in the production of refined Cu. The main benefits of using Cu scrap are (i) enables higher energy efficiency compared to mining and processing Cu ore, (ii) avoids emissions, (iii) circumvents wastes from mining, concentration, leaching and smelting stages, and (iv) lessens ore depletion and improves overall copper availability [10].

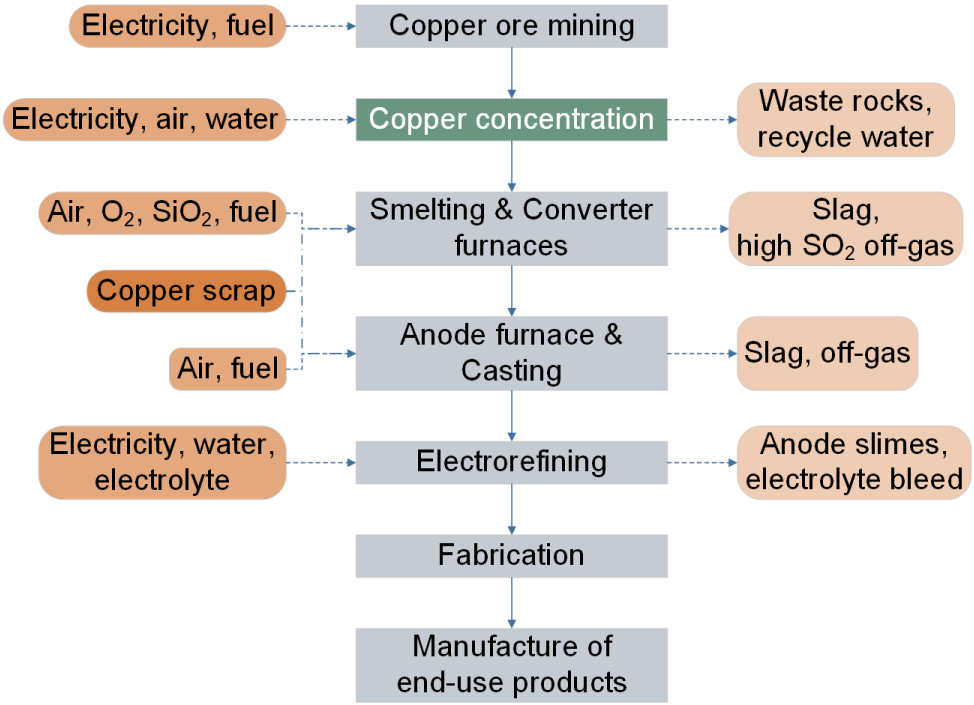

Figure 1. Pyrometallurgical production processes within the Cu value chain

The mining and concentration stages together account for about 65 – 80% of the total emissions from mine-to-copper cathode production. In addition, the flash smelting technology used in the pyrometallurgical route accounts for roughly 60% of primary Cu production [11]. However, as ore grades decline and concentrate quality becomes more heterogeneous, maintaining stable flash smelter operation becomes increasingly difficult, with adverse impacts on throughput, specific energy consumption and CO_2 emissions [12]. The most common copper-containing minerals are chalcopyrite ($CuFeS_2$) and chalcocite (Cu_2S), but their concentrations in the ore are low, ranging from 0.3 – 1.7 wt.% Cu [13]. In addition, typical Cu ore concentrates that are fed to smelters primarily contain $CuFeS_2$, iron sulfide (FeS_2), copper sulfide (CuS) and Cu_2S, with exact compositions depending on the source of ore [14]. Therefore, enhancing the quality of Cu concentrate before it enters the smelter is an attractive lever for decarbonization, as well as for improving operational stability and process efficiency. In this work we focus on developing particle scale models for a model compound present in copper concentrate and its reaction with hydrogen (H_2).

To date, modeling advances of pyrometallurgical Cu refinement have mainly targeted the smelting furnace, with particular focus on flash smelting furnaces (FSF). A thermodynamic model was developed by Li et al. [15] for Cu side-blown smelting to accurately predict the product composition and the distribution behavior of impurity elements under representative operating conditions. Solghar et al. [16] developed a thermochemical model of the FSF, assuming that all matte, slag, dust and gas phases were in thermal and chemical equilibriums and determined that rate of fuel consumption was heavily influenced by the variation in working parameters of the furnace. In addition, computational fluid dynamics (CFD) has been used to study the Cu FSF, with Kumar et al. [17] investigating the impact of process parameters on smelting operation considering the model domains as the reaction shaft and settler freeboard. Zhou et al. [18] utilized CFD to investigate how gas flows influence particle dispersion and combustion in copper FSF, revealing that large momentum ratio combined with large amounts of air was beneficial in dispersion of particles and led to quicker combustions. Urbaniak et al. [19] developed a model to investigate copper concentrate roasting within a fluidized bed-furnace during the smelting process, establishing that a deposit with 40 mm thickness determined a reduction by 80% in the absorbed energy by water from the bed. Furthermore, Zhu et al. [20] employed discrete element method (DEM) modeling to study segregation of copper concentrate particles in the feeding system of a FSF, highlighting that its reduction was possible by increasing sloping angle or narrowing chute width.

Since most published models on pyrometallurgical Cu refinement focus on the smelting stage, the pre-treatment of Cu ores to improve concentrate grade for smelting remains largely unexplored. In the current work, this gap is addressed by developing a particle-scale modeling framework for hydrogen-assisted desulfurization and upgrading of Cu concentrates, designed to be later coupled with reactor-scale simulations. Overall, this study provides (i) a validated CFD multilayer particle model for Cu_2S conversion using H_2, (ii) insight into coupled transport-reaction behavior within pellets that account for dynamic porosity, and (iii) optimization-based identification of operating windows to enhance Cu_2S conversion while improving H_2 utilization.

MODEL DEVELOPMENT

The current study considered Cu_2S as the representative copper sulfide component to establish a baseline and enable validation using available kinetic data for desulfurization of copper sulfates with H_2. Further implementation of model kinetics to other components will be extended to mixed phases once consistent kinetics are available. As such, a 2D CFD multilayer particle model was developed in COMSOL Multiphysics 6.3 to study the desulfurization of Cu_2S by H_2, leading to the following overall reaction between ore and H_2 (Eq. (1)):

$$Cu_2S\,(s) + H_2\,(g) \rightarrow 2Cu\,(s) + H_2S\,(g) \qquad \Delta H^0_{298} = +60\ kJ/mol \qquad (1)$$

Model kinetics

The intrinsic kinetics of hydrogen reduction of Cu_2S were studied by Sohn and Won [21], who derived a first-order reaction rate with respect to the solid reactant and H_2 concentrations. The experimental measurements were carried out at temperatures between 823 – 1023 K in a thermogravimetric analyzer. The reaction kinetics were measured using small particles to neglect interparticle diffusional effects, as well as thin pellets of various sizes and thickness values to ensure diffusional effects were minimal. The activation energies obtained from experiments with both powder and pellets were 92 kJ/mol, while the pre-exponential factor (k_0) was around two times higher for the porous pellets than the powder as an effect of increased surface area. Thus, the rate of conversion for the dense Cu_2S particles during H_2 reduction was expressed as Eq. (2), with k_0 as $2.23 \cdot 10^6$:

$$\frac{dX_{Cu_2S}}{dt} = k_0 \cdot e^{\left(-\frac{11{,}100}{T}\right)} \cdot c_{H_2} \cdot \left(1 - X_{Cu_2S}\right) \qquad (2)$$

Model geometry and mesh

The model consisted of two domains: a fluid domain representing the interstitial gas and a particle domain representing the solid ore (Figure 2). The transport of species was solved over time for both domains and was coupled with a momentum balance that was solved under steady-state conditions for the gas phase. The pellet bed, with a diameter of 3 cm, was represented by a single layer of particles in the radial direction and multiple layers in the axial direction. The pellets were positioned to maximize the contact area between particles and incoming reacting gas front (i.e., H_2), while respecting the prescribed bed porosity of 0.3 (i.e., void space). In addition, to avoid artificial boundary effects, fluid-only sections were implemented with the thickness of one particle layer at the inlet and outlet of the model domain.

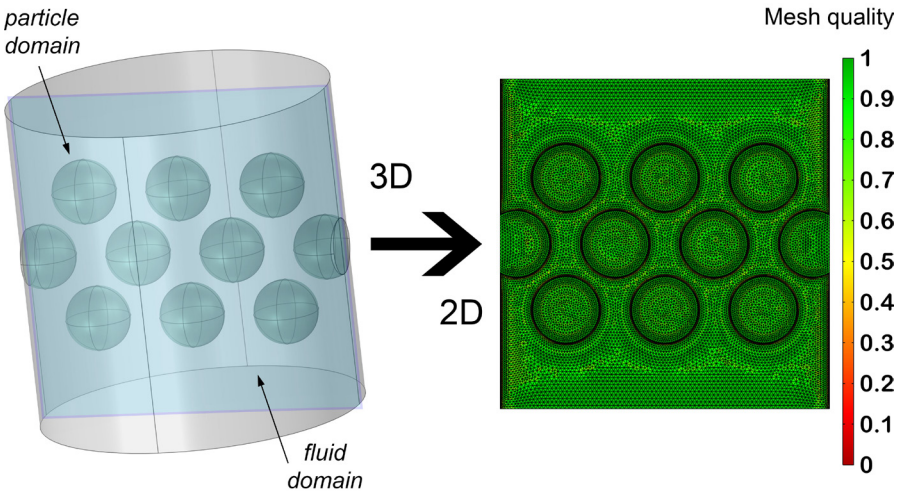

Figure 2. 3D to 2D geometry transition and 2D mesh quality (i.e., 1 meant best possible element)

To reduce model complexity, the initial 3D domain was sectioned and converted into a 2D particle-fluid model, significantly lowering the degrees of freedom and enabling investigation of operating conditions by optimization within reasonable computational times. In addition, since the dominant gradients were along the direction of flow and the bed structure was homogeneous in the out-of-plane direction, little accuracy was lost by neglecting the third dimension, while the essential transport and reaction phenomena were still captured. Mesh convergence was assessed based on the predicted pressure drop,

reaching a final mesh with 36,886 elements and an average element quality of 0.83, as indicated by the distribution shown in Figure 2, where quality was represented in terms of a dimensionless value between 0 (i.e., degenerated element) and 1 (i.e., best possible element).

Model parameters and operating conditions

The main operating conditions and parameters considered in this work are shown in Table 1. The simulations were based on the experimental conditions for which Sohn and Won [21] carried out their investigation on Cu_2S reduction by H_2.

Table 1. Operating conditions and parameters used in the particle model

Parameter	Value	Parameter	Value
Temperature	823 – 1023 [K]	Sample mass	20 – 60 [mg]
Gas pressure	0.86 [atm]	Pellet porosity	0.22 [-]
Flow rate	0.1 [dm^3/min]	Pellet diameter	3.11 [mm]

Model assumptions

The main assumptions considered when developing the multilayer particle model are shown below:

· The solid pellet ores were entirely composed of Cu_2S.
· The pellets were spherical with constant radii throughout the reaction.
· Diffusion was modeled using Fick's law with effective diffusivities.
· Incompressible laminar fluid flow was assumed for the gas phase.
· Isothermal conditions were assumed.

Model equations

The equations implemented in the 2D multilayer particle model are presented in Table 2. Species transport in the fluid domain was described by a time-dependent convection-diffusion equation (Eq. (3)), assuming Fickian diffusion with no reaction in the gas phase. Transport of gas species in the pellet domain was modeled by a diffusion-reaction equation (Eq. (4)), with effective diffusion (D_e) calculated using a Millington and Quirk relation, while the reaction rate term used the kinetics published by Sohn and Won [21] (Eq. (2)). Species transport for the solid components (Eq. (6)) only included a reaction term. The coupling between fluid and particle domains was implemented through a mass transfer boundary condition (Eq. (7)) at the interface, where

the mass transfer coefficient ($k_{m,i}$) was evaluated from the Sherwood number, diffusion coefficient and particle radius. Particle porosity was transiently calculated (Eq. (9)) by accounting for a shrinkage factor, estimated with the molar volumes of the solid components, and the conversion of the Cu_2S reactant. The Navier-Stokes equations in the x and y directions, coupled with the continuity equation, were used to describe momentum transport in the fluid domain. A stationary study solved incompressible laminar flow for the fluid domain, with Reynolds numbers confirming laminar flow in all cases, resulting in a velocity field that provided the convective term for the transient species transport, allowing the change of compositions for gas and solid components to be resolved in time. Consequently, the convective transport in the particles was assumed negligible and species transport was solved solely by diffusion-reaction.

Table 2. Equations implemented in the CFD multilayer particle model

Species transport in the fluid domain	
$\frac{\partial c_i}{\partial t} - \frac{\partial}{\partial x}\left(D_i \frac{\partial c_i}{\partial x}\right) - \frac{\partial}{\partial y}\left(D_i \frac{\partial c_i}{\partial y}\right) + u_x \frac{\partial c_i}{\partial x} + u_y \frac{\partial c_i}{\partial y} = 0$	(3)
Species transport in the pellet domain (for gas and solid phases)	
$\varepsilon_p \frac{\partial c_{i,p}}{\partial t} - \frac{\partial}{\partial x}\left(D_{e,i} \frac{\partial c_{i,p}}{\partial x}\right) - \frac{\partial}{\partial y}\left(D_{e,i} \frac{\partial c_{i,p}}{\partial y}\right) = R_i$	(4)
$D_{e,i} = \varepsilon_p^{4/3} \cdot D_i$	(5)
$(1 - \varepsilon_p) \frac{\partial c_{s,i}}{\partial t} = R_i$	(6)
$J_{i,p} = k_{m,i} \cdot (c_i - c_{i,p})$	(7)
$k_{m,i} = \frac{Sh \cdot D_i}{r_p}$	(8)
$\varepsilon_p = \varepsilon_{p,0} + \left(1 - \varepsilon_{p,0}\right) \cdot (1 - \Phi) \cdot X_{Cu_2S}$	(9)
$\Phi = \frac{2 \cdot V_{M,Cu}}{V_{M,Cu_2S}}$	(10)
Momentum transport in the fluid domain	
$\rho_f \left(u_x \frac{\partial u_x}{\partial x} + u_y \frac{\partial u_x}{\partial y}\right) = -\frac{\partial p}{\partial x} + \mu_f \left(\frac{\partial^2 u_x}{\partial x^2} + \frac{\partial^2 u_x}{\partial^2 y}\right)$	(11)
$\rho_f \left(u_x \frac{\partial u_y}{\partial x} + u_y \frac{\partial u_y}{\partial y}\right) = -\frac{\partial p}{\partial y} + \mu_f \left(\frac{\partial^2 u_y}{\partial x^2} + \frac{\partial^2 u_y}{\partial^2 y}\right)$	(12)
$\frac{\partial u_x}{\partial x} + \frac{\partial u_y}{\partial y} = 0$	(13)

Optimization study

A constrained optimization study was carried out to identify the operating conditions necessary to enable efficient desulfurization while preventing solid thermal degradation. The goal was to maximize overall hydrogen utilization with high Cu_2S conversion by identifying the optimal inlet hydrogen mole fraction and operating temperature as decision variables. The gradient-free Nelder-Mead method was chosen to solve the optimization problem with an optimality tolerance of 0.01 and 1000 maximum number of evaluations. Nelder-Mead is a derivative-free optimization method that considers a simplex of N+1 points, where N is the number of control variables, to perform reflections, expansions and contractions. This improves the worst point in the control variable space, and, consequently, the objective function. The main benefits to using Nelder-Mean in the current study were that (i) the simplex required less computational time than other-gradient free methods [22], and (ii) it was suitable due to the small number of decision variables in the objective function (i.e., 2).

RESULTS AND DISCUSSION

The multilayer model was validated using the experimental measurements presented by Sohn and Won [21]. Figure 3 shows experimentally measured Cu_2S conversion in time as function of time at various temperatures between 823 – 1023 K and a flowrate of 2 dm^3/min. Across all cases, higher overall conversion was achieved in less time at higher temperatures. The model reproduced the experimental conversion data well over the full temperature range with values for R^2 (coefficient of determination) higher than 0.9 and *RMSE* (root mean square error) values between 0.014 – 0.024 for conversion of Cu_2S.

Table 3. Accuracy of predicted conversion for variable temperatures

T [K]	823	868	921	973	1023
R^2	0.904	0.984	0.996	0.993	0.994
RMSE	0.022	0.015	0.014	0.024	0.022

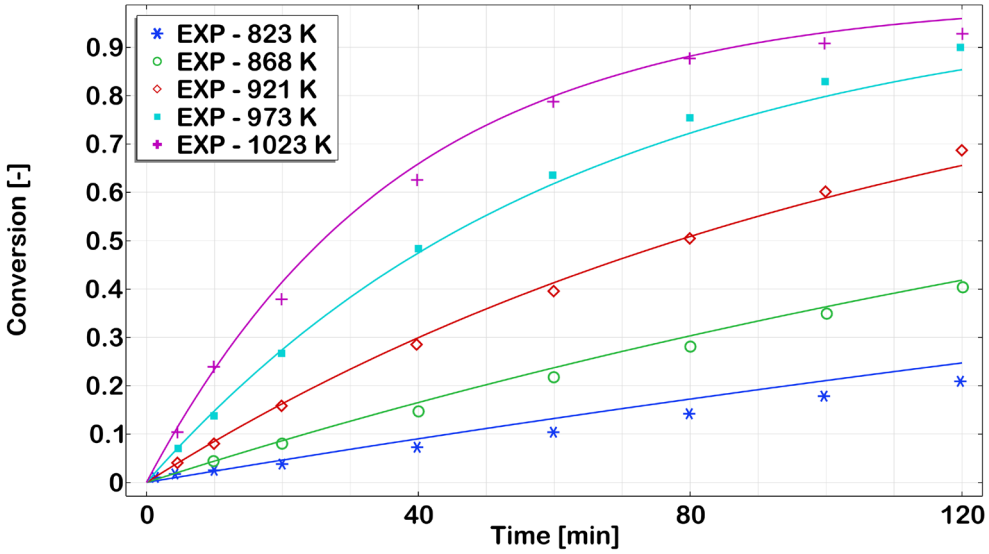

Figure 3. Experimental measurements [21] vs. CFD model predictions (lines) for conversion of Cu_2S in time at variable temperatures

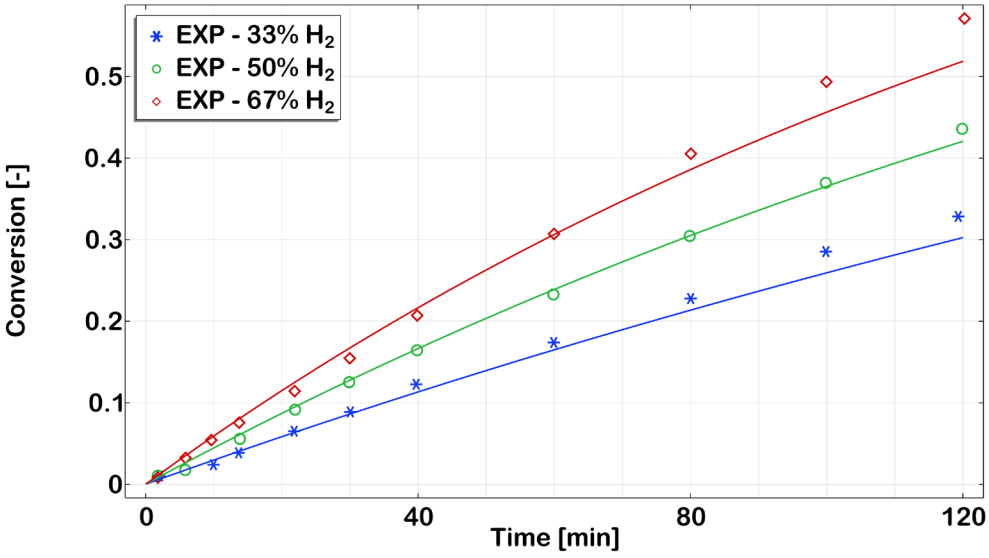

Figure 4. Experimental measurements [21] vs. CFD model predictions (lines) for conversion of Cu_2S in time at variable H_2 concentrations

Figure 4 shows experimentally measured Cu_2S conversion in time as function of three H_2 concentrations: 33%, 50% and 67%. The H_2 concentration was controlled using inert He gas, the total flowrate for the two components being 12 dm^3/min. Across all cases, higher overall conversion was achieved in less time at higher H_2 concentrations. The model exhibited good fit between measurements and predictions by yielding values for R^2 higher than 0.9 and *RMSE* values between 0.006 – 0.021 for conversion of Cu_2S.

Table 4. Accuracy of predicted conversion variable H_2 concentrations

cH_2 (%)	33	50	67
R^2	0.983	0.997	0.987
RMSE	0.013	0.006	0.021

Figure 5 presents the pressure loss distribution in the 2D particle-fluid domain. A gradual pressure drop was noticed closer towards the particle domains, while within the particle region, higher loss was seen around the narrow gaps between pellets. Overall, a small total pressure loss was predicted across the pellet domain, as expected for low-Reynolds laminar flow.

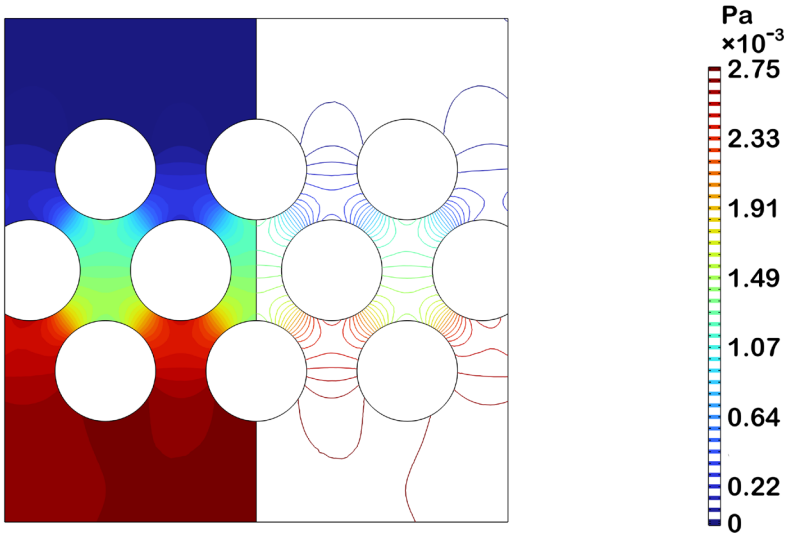

Figure 5. CFD model predicted pressure drop distribution

Figure 6 presents the velocity magnitude and streamlines in the 2D particle fluid domain. A fully developed laminar flow boundary condition was assumed at the inlet section. The narrow gaps between the pellets determined an acceleration of flow, reaching the highest velocities in these constricted areas, while a low-velocity zone was formed in the wakes. The streamlines illustrated the path of flow and indicated that no recirculation zones were formed, as expected for low-Reynolds laminar flow.

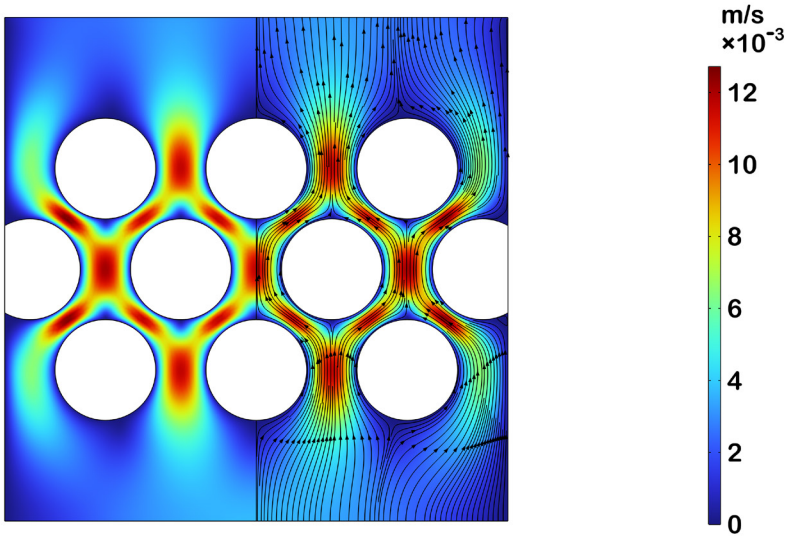

Figure 6. CFD model predicted velocity profile

Figure 7 presents the evolution in time of relative concentrations (i.e., gas concentration at time *t* for component *i* divided by total inflow concentration of gas) for all gas and solid components. The left panels show the gas-phase concentrations of H_2 and H_2S in the fluid-particle domains, while the right panels present the solid-phase concentrations of Cu_2S and Cu inside the pellets at different simulated times. At 0 s, before any gas was introduced to the domain, the pellet consisted entirely of Cu_2S. Over time, the H_2 gas penetrated the pellets forming H_2S, which then diffused through the particles toward the fluid domain. The Cu_2S depleted gradually from the outer regions where the H_2 diffused toward the pellet cores, with Cu being produced correspondingly from the surface inward.

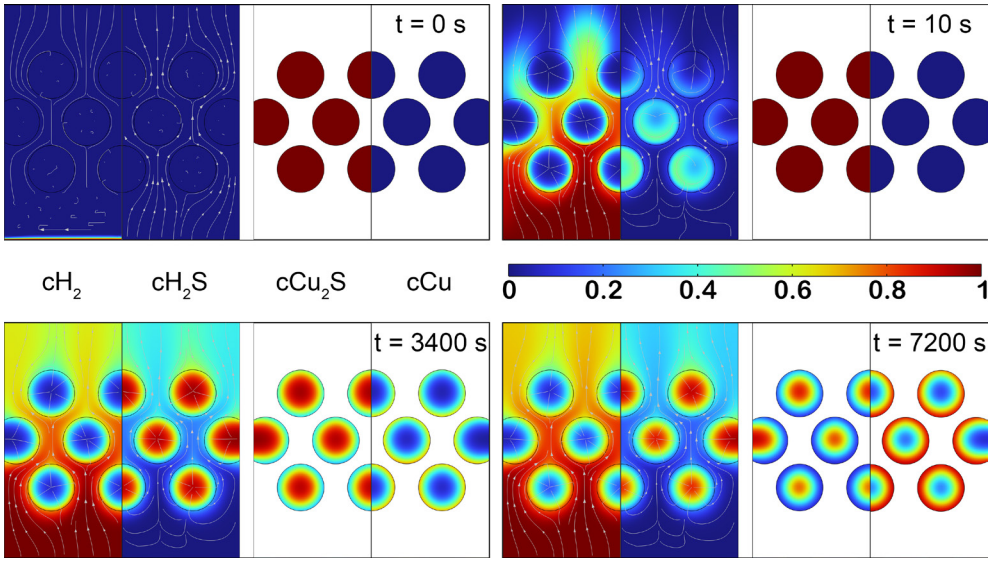

Figure 7. CFD model predicted concentration evolution for gases and solids

Figure 8 illustrates the change of particle porosity over time for a particle situated in the center of the fluid domain. The initial porosity was assumed to be completely uniform at 0.22 (i.e., void space). Shortly after H_2 penetration, a slight porosity change was seen at the edges, where reaction first took place. Further into the reduction reaction at 3600 s, a strong porosity gradient developed, with high porosity noticed in the outer shell, while porosity in the less reacted core barely changed. At 7200 s, the porosity increased throughout the entire pellet, forming a more compact inner region, reflecting the shrinkage of solid volume due to the progression of conversion inward toward the pellet core.

A multi-parameter optimization was performed to maximize a combined objective function (Eq. (14)) considering the average conversion of Cu_2S and overall hydrogen utilization. Two decision variables were considered: (i) inlet hydrogen mole fraction (y_{in,H_2}) and (ii) operating temperature (T) with an upper limit of 973 K imposed to avoid Cu sintering, observed to take place in the experimental measurements at higher temperatures [21].

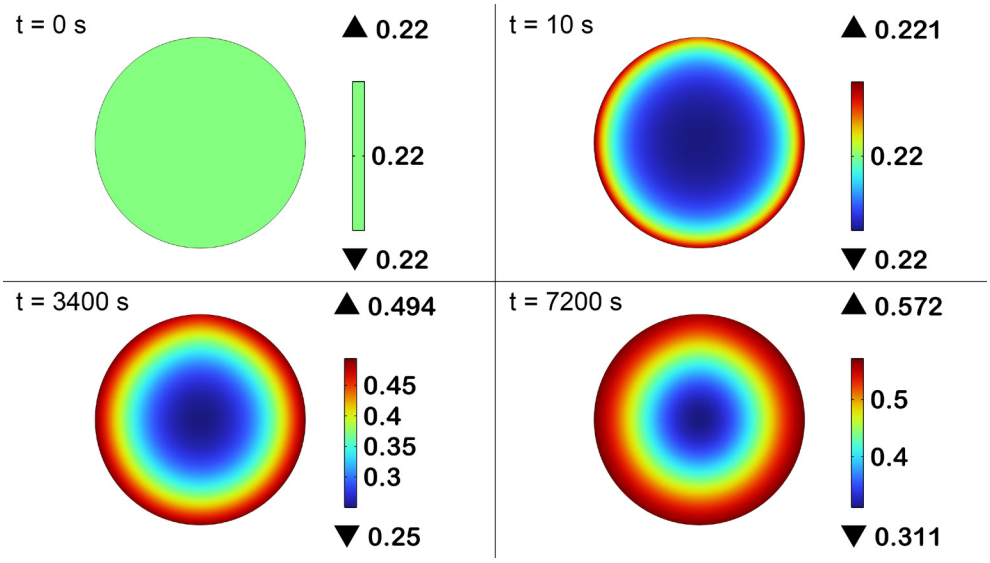

Figure 8. CFD model predicted pellet porosity change

The product form in the objective function (Eq. (14)) served to measure simultaneous improvement, such that *J* became high only for both high Cu_2S conversion and H_2 utilization, rather than for one term high and the other poor (e.g., high conversion but large H_2 slip). In addition, since *J* could become zero if either term approached zero, the form prevented reporting an optimal solution in which one key performance indicator collapsed to an unacceptable value (i.e., zero).

$$\max_{y_{in,H_2},T} J = \left(1 - \frac{c_{H_2}}{c_{in,H_2}}\right) \cdot \left(1 - \frac{w_{Cu_2S}}{w_{0,Cu_2S}}\right) \tag{14}$$

Subject to:

$$0.33 \leq y_{in,H_2} \leq 1$$
$$823\ \mathrm{K} \leq T \leq 973\ \mathrm{K}$$

The representative points of the converged optimal solutions are presented in Table 5. The two terms considered in the combined objective function Eq. (14) were intended to represent process performance (i.e., Cu_2S conversion) and resource efficiency (i.e., H_2 utilization). Generally, these two

quantities could be in trade-off: increase in H_2 driving force (i.e., higher H_2 inlet fraction) typically increases conversion based on the kinetic relationship published by Sohn and Won [21], but could also lead to unreacted H_2 in the outlet if the gas-solid contact time and transport limitations (i.e., high internal particle diffusion) prevented complete consumption of the reactant. However, within the parameter window considered here, matching the experimental conditions used for model validation, the combined objective function increased monotonically, resulting in a boundary solution as the optimal solution, rather than an interior optimum. Across all temperatures, the objective function increased consistently with y_{in,H_2}, indicating a strong dependence of reduction kinetics on H_2 availability. Higher H_2 partial pressure enhanced both fluid-particle interfacial transport and intraparticle reaction rates. In addition, the objective function also increased with temperature, enhancing reaction kinetics, which led to better conversion and improved H_2 usage. The highest value of the objective function achieved was 0.0705 obtained at 100% H_2 inflow composition and 973 K.

Although the temperature was allowed to vary between 823 – 973 K, the values reported in Table 5 correspond to the converged optimal solutions. To confirm that the solutions were not artifacts related to the initial simplex, the Nelder-Mead algorithm optimization was carried out using multiple starting points within the feasible temperature (i.e., 823 – 973 K) and hydrogen molar fraction (i.e., 0.33 – 1) boundaries. All runs converged to the same optimal conditions, indicating a global optimum, consistent with the steady increase of the objective function with temperature.

Table 5. Representative solutions calculated during optimization

Number	Variable 1 y_{in,H_2} [-]	Variable 2 T [K]	Objective function J
1	0.33	898	0.012
2	0.67	898	0.021
3	1.00	898	0.031
4	1.00	917	0.040
5	1.00	937	0.050
6	1.00	956	0.060
7	1.00	973	0.070 (optimum)

Figure 9 shows the change in time of H_2 utilization (U_{H_2}), the first term in Eq. (14), and Cu_2S conversion. A rapid decrease in U_{H_2} from 1 was noticed as H_2 was being consumed entirely, followed by a gradual approach to a low

value as H_2 slip increased, ending at 0.23 after 3600 s. In contrast, the Cu_2S conversion increased steadily, reaching 0.29 after 3600 s. The shape of the curves confirmed the expected interplay between reaction-diffusion within the pellets and illustrated the trade-off between minimizing H_2 slip and maximizing solid conversion.

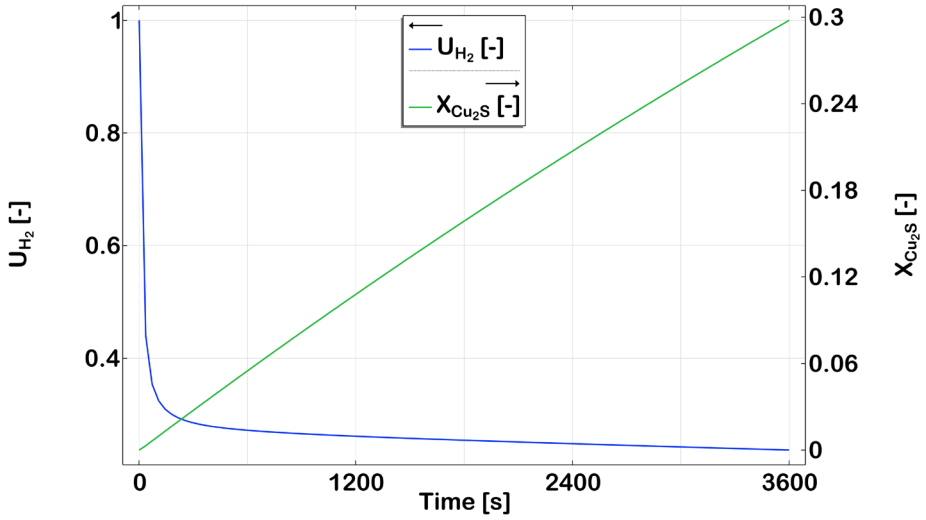

Figure 9. Evolution in time of the objective function during optimization

CONCLUSIONS

A 2D CFD multilayer particle model was developed to describe hydrogen-driven desulfurization of Cu ore concentrate, considering Cu_2S as the representative solid phase. The model coupled velocity and pressure profiles in the fluid domain to transiently solved species transport for both gas and solid components based on kinetic rates for desulfurization published by Sohn and Won [21], while also accounting for change of pellet porosity in time.

The model was validated with experimental data from literature [21], yielding R^2 coefficients higher than 0.9 and low *RMSE* values, thus confirming an accurate representation of the intraparticle diffusion-reaction mechanisms. The simulations solved spatial gradients for gas composition, solid conversion and porosity within the particle, as well as interstitial gas velocity and pressure fields, reflecting a limited decrease in total pressure through the multiplayer particle domain, as expected for the low-Reynolds laminar flow considered in this work.

An optimization study was conducted to identify the optimal inlet H_2 molar fraction and operating temperature necessary to maximize a combined objective function of H_2 utilization and Cu_2S conversion. The results demonstrated that both higher temperature and higher inlet mole fraction strongly promoted conversion and H_2 usage. The maximum was achieved at 100% H_2 and 973 K, highlighting the trade-off between maximizing conversion and minimizing H_2 slip.

The modeling framework developed in this work can be directly extended and coupled with reactor-scale CFD and process integration studies to support decarbonization of primary copper production. Overall, the results support decarbonization by identifying conditions that minimize H_2 slip, thus reducing upstream emissions associated with hydrogen production (e.g., GHGs to generate electricity for electrolysis) per t of Cu in hydrogen-based desulfurization.

ACKNOWLEDGMENTS

This research was supported by More4LessCu project (CETP-FP-2023-00394) which is funded within the Clean Energy Transition Partnership (CETP) programme, co-funded by the European Union. And was supported by a grant from the Ministry of Research, Innovation and Digitization, CNCS/CCCDI - UEFISCDI, project number ERANET-CETP-More4LessCu, within PNCDI IV.

NOMENCLATURE

c_i – concentration of species *i,* gas phase, fluid domain [mol/m^3]

$c_{i,p}$ – concentration of species *i,* gas phase, particle domain [mol/m^3]

$c_{s,i}$ – concentration of species *i,* solid phase, particle domain [mol/m^3]

D_i – molecular diffusion coefficient in the fluid domain [m^2/s]

$D_{e,i}$ – effective diffusion coefficient in the pellet [m^2/s]

J – objective function [-]

$J_{i,p}$ – mass flux across particle-fluid interface [kg/m^2/s]

k_0 – pre-exponential factor [m^3/mol/s]

$k_{m,i}$ – mass transfer coefficient of species *i* for film resistance [m/s]

p – relative pressure [Pa]

r_p – particle radius [m]

R_i – reaction rate term [mol/m^3/s]

R^2 – coefficient of determination [-]

Sh – Sherwood number [-]

t – time [s]

T – temperature [K]

u, v – gas velocity components in the x and y directions [m/s]

U_{H_2} – hydrogen utilization [-]

$V_{M,i}$ – molar volume of solid species i [m^3/mol]

x, y – spatial coordinates in the 2D domain

X_{Cu_2S} – conversion of solid component Cu_2S [-]

y_{in,H_2} – inlet hydrogen mole fraction [-]

ε_p – particle porosity (i.e., void space) [-]

Φ – shrinkage factor [-]

μ_f – fluid dynamic viscosity [Pa·s]

ρ_f – fluid density [kg/m^3]

CFD – computational fluid dynamics

GHG – greenhouse gas

RMSE – root mean square error

REFERENCES

1. International Energy Agency (IEA); Global Energy Review 2025, Paris, **2025**
2. M. Crippa; D. Guizzardi; F. Pagani; M. Banja; M. Muntean; GHG emissions of all world countries – 2025 Report, Luxembourg, **2025**
3. The Copper Mark (TCM); Decarbonizing the Copper Sector – Discussion Topics and Considerations for a 1.5 °C-aligned Trajectory and Target-setting Methodology, **2024**
4. T. Watari; S. Northey; D. Giurco; S. Hata; R. Yokoi; K. Nansai; et al.; Resources, Conservation and Recycling, **2022**, 179, 106118
5. International Copper Association (ICA); Copper — The Pathway to Net Zero, **2023**
6. S&P Global; The Future of Copper: Will the Looming Supply Gap Short-Circuit the Energy Transition?, **2022**
7. The Copper Mark (TCM); Decarbonizing the Copper Sector – Discussion Topics and Considerations for a 1.5 °C-aligned Trajectory and Target-setting Methodology, **2024**
8. International Copper Study Group (ICSG); The World Copper Factbook 2025, **2025**
9. International Finance Corporation (IFC); Net Zero Roadmap for Copper and Nickel Mining – Technical Report, **2023**
10. M. Chen; D. Sukhomlinov; P. Taskinen; J. Hamuyuni; M. Tiljander; M. Lindgren; et al.; Metallurgical and Materials Transactions B, **2025**, 56, 1897–1913
11. M. Li; Y. Feng; X. Chen; Metals, **2024**, 14, 840

12. A. A. Solghar; M. Abdolzadeh; Proceedings of the Institution of Mechanical Engineers, Part E: Journal of Process Mechanical Engineering, **2015**, 229, 11–24
13. S. Nirmal Kumar; B. Desai; V. Tathavadkar; Y. Patel; J. Patel; A. Singh; et al.; Mineral Processing and Extractive Metallurgy, **2023**, 132, 49–61
14. J. Zhou; J. Zhou; Z. Chen; Y. Mao; JOM, **2014**, 66, 1629–1637
15. R. Urbaniak; B. Hadała; R. Stanik; J. Konstanty; A. Olejnik; International Communications in Heat and Mass Transfer, **2024**, 108284
16. Z. Zhu; P. Zhou; Z. Chen; Z. Xiao; D. Wu; S. Kuang; Powder Technology, **2024**, 443, 119898
17. M. E. Schlesinger; K. C. Sole; W. G. Davenport; G. R. F. Alvear Flores; Extractive Metallurgy of Copper, 6th ed.; Elsevier, **2021**, 1–573
18. V. M. Sanchez-Corrales; J. A. Valera-Gonzalez; P. Flores-Perez; M. Perez-Tello; JOM, **2004**, 56, 29–32
19. H. Y. Sohn; S. Won; Metallurgical Transactions B, **1985**, 16, 831–839